JES Focus Issue on Advances in Modern Polymer Electrolyte Fuel Cells in Honor of Shimshon Gottesfeld

Atomic Layer Deposition of Pt Nanoelectrode Array for Polymer Electrolyte Fuel Cells

Dinesh C. Sabarirajan,[1] Thomas Y. George,[2] James Vlahakis,[1] Robert D. White,[1] and Iryna V. Zenyuk[1,2,3,*,z]

[1]*Department of Mechanical Engineering, Tufts University, Medford, Massachusetts 02155, USA*
[2]*Department of Chemical and Biological Engineering, Tufts University, Medford, Massachusetts 02155, USA*
[3]*Department of Chemical and Biomolecular Engineering, National Fuel Cell Research Center, University of California, Irvine, Irvine, California 92697, USA*

This study presents thin-film electrode design for polymer electrolyte fuel cells (PEFCs) prepared by atomic layer deposition (ALD). Due to structural alignment and controlled pore sizes, this Pt ALD nanoelectrode array is a promising model ionomer-free electrode for transport and reaction kinetics studies. The ALD fabrication process is used to deposit monolayers of Pt onto a sacrificial substrate by dissociative chemisorption in a self-assembling reaction. A novel thermal exposure mode is used to deposit Pt nanostructures onto anodized aluminum oxide (AAO) discs using trimethylcyclopentadienylmethylplatinum (IV) and oxygen gas as precursors. This technique provides additional time for surface reactions and allows higher penetration of the precursor into the AAO disc. By varying exposure time the electrode thickness is varied. The model electrode is used with metallic gold interlayer and varied relative humidity to delineate ion transport mechanisms during detection of electrochemical surface area with cyclic voltammetry (CV) and CO-stripping. This study shows that adsorbed hydrogen surface diffusion is an unlikely transport mechanism during CV and that proton surface migration is a more feasible mechanism.
 [DOI: 10.1149/2.0091907jes]

Manuscript submitted November 19, 2018; revised manuscript received February 19, 2019. Published March 15, 2019. This was Paper 2491 presented at the Honolulu, Hawaii, Meeting of the Society, October 2–7, 2016. *This paper is part of the JES Focus Issue on Advances in Modern Polymer Electrolyte Fuel Cells in Honor of Shimshon Gottesfeld.*

Polymer electrolyte fuel cells (PEFCs) offer high power density compared to other electrochemical energy conversion devices. To achieve broad commercialization, they must overcome several technological barriers. The major hurdle is the high cost associated with the use of platinum (Pt) as an electrocatalyst. The state-of-the-art PEFCs' conventional carbon-supported platinum (Pt/C) electrodes currently use about 0.25 mg/cm^2 of Pt loading on the cathode, whereas the set target for 2020 by the U.S. Department of Energy (DOE) is 0.125 mg/cm^2. Thin-film electrodes have potential to meet this requirement due to effective Pt utilization.[1–6] 3M's nano-structured thin-film electrodes (NSTF) have shown good durability at start-stop and voltage cycling,[7] as well as high specific activity and specific rated power.[7,8] The NSTF electrodes are fabricated by sputtering a thin film of Pt onto high surface-area organic pyrelene red whiskers. The advantages of this fabrication technique are reduced Pt loading, as the 0.5 μm thick NSTF electrodes use less than 0.15 mg$_{Pt}$/cm^2, and electrochemical stability, as there is no carbon corrosion.[8–10] The proton transport mechanisms under the range of operation conditions are very poorly understood because it is difficult to isolate PEFC's polarization losses due to poor proton conductivity vs. mass-transport losses (flooding). In the NSTF electrodes, as well as in the other thin-film ionomer-free electrodes, the hydrophobic backbone of Nafion is absent. Under operation conditions, where water transport through evaporation is limited (cool-wet condition), severe flooding occurs due to the hydrophilic nature of Pt and the low water-storage capacity of thin-film electrodes.[11–14] Although flooding is undesirable, condensed water films on the Pt surface are needed for ion transport.[15] Hu et al. have shown that for Pt black electrodes without ionomer, PEFC's polarization significantly depends on relative humidity (RH).[16]

Generally, ionic conductivity is a function of the number of charge carriers and their mobility. In electrodes containing ionomer, both numbers are high, whereas in deionized water, the ion concentration is ∼7 orders of magnitude lower than that in a polymer electrolyte such as Nafion. In ionomer-free electrodes, such as Pt-black or NSTF electrodes, water assists in ion conduction and one might expect ionic conductivity to be close to deionized (DI) water. However, ionic conductivity of ionomer-free electrodes was measured to be 2–3 orders of magnitude higher than DI water.[12,17] These findings suggest that in porous high surface area electrodes, confinement and local electric fields increase ion concentration and/or ion mobility. Several experimental and modeling studies propose two ion transport mechanisms: 1) H$_{ad}$ surface diffusion[18–22] and 2) water-mediated proton conduction.[10,15,23,24] To understand these mechanisms, model electrodes with controlled geometry and active area must be designed.

In this study, atomic layer deposition (ALD) was used to fabricate thin-film model electrodes. The ALD gas-phase fabrication process provides a uniform and conformal Pt layer with precise thickness on high aspect-ratio substrates. The ALD process applied to fuel cells is relatively new; several works reported electrodes' performance in rotating disk electrode (RDE) experiments but few included tests in the PEFC hardware. Only two publications have reported fuel cell power densities using electrodes fabricated by the ALD process: one on a sacrificial substrate,[2] another on nano-fibers,[3] and both using Plasma Enhanced (PE) ALD. However, PEALD results in limited conformity of deposited films. This is caused by the de-activation of plasma radicals in high aspect-ratio structures, which leads to a deposition depth of only 2 μm.

Here, we fabricate Pt electrodes with a novel thermal ALD process. By varying exposure time, thickness of the electrode is controlled. The activity and performance of the deposited electrodes with varied exposure times is characterized in a membrane electrode assembly (MEA) fuel cell setup under various relative humidities (RH) and operating potentials. The electrochemical surface area (ECSA) is assessed with both cyclic voltammetry and CO-stripping to probe electrocatalyst accessibility with H$_{upd}$ and CO. Furthermore, gold interlayers are added to the MEA to switch on and off different ion transport mechanisms, separating H$_{ad}$ surface diffusion from charged proton surface migration.

Experimental

Material synthesis.—The nanoelectrode arrays were fabricated with a novel ALD thermal exposure technique using a Cambridge

*Electrochemical Society Member.
[z]E-mail: iryna.zenyuk@uci.edu

Nanotech Savannah ALD system. Anodized aluminum oxide (AAO) discs (patented by Whatman Ltd., manufactured by Sigma Aldrich) with 13 mm diameter and 100 nm and 200 nm pore sizes were used as the templates for fabricating the nanoelectrode arrays.[2,25,26] These discs were placed equidistant in stainless steel baskets to have maximum exposure to the precursors in a chamber that was maintained at 250°C with gas valve manifolds held at 150°C. The precursors used to fabricate the Pt nanoelectrode arrays were trimethyl (methylcyclopentadienyl) platinum (IV) ((MeCpPt)Me_3) (Strem Chemicals Inc.) and UHP oxygen gas (Airgas). The (MeCpPt)Me_3 precursor was preheated to 75°C and stabilized for at least one hour before the deposition process. Thermal mode ALD provides additional time for the precursor gases to diffuse into the pores of the AAO discs. The technique enables electrode thickness of up to 10 μm for 500 cycles.

AAO discs with 200 nm pore diameters and 13 mm disc diameters were used as the base case substrates for the deposition. Oxygen gas was pulsed for 0.015 s, after which the chamber was isolated from the purge gas for 5 s. During the 5 s period, the oxygen precursor adsorbed on AAO discs, creating additional sites for Pt nucleation during (MeCpPt)Me_3 precursor pulsing. After the exposure time, the excess gas was purged by introducing nitrogen gas into the chamber at a flow rate of 3 sccm for 10 s. Then, the (MeCpPt)Me_3 precursor was pulsed for 0.015 s and the deposition chamber was isolated by closing the manifold valve. For the base-case a 5 s exposure time followed, allowing precursor to adhere to the active sites created by oxygen. The excess (MeCpPt)Me_3 precursor gas was removed by purging the chamber with nitrogen gas for 10 s, as before. This process was repeated for 500 cycles for monolayer by monolayer deposition of Pt into the pores of the AAO disks. For AAO disks with 100 nm pore diameters, the experiment was repeated, using 300 deposition cycles. The loading was measured by subtracting the weight of the pristine AAO discs from the weight of discs with Pt. Area of the ALD deposition on the disc was accounted for as well. Each sample was weighed separately before being hot-pressed and etched to be made into an MEA.

The Pt nanoelectrode array with a layer of Au was fabricated by sputtering Au onto the Pt ALD electrode using the NSC 3000 Sputter tool, where an electron beam with 150 W power was shot onto a gold target and Au was deposited onto the electrode. The thickness of the sputtered Au layer was 100 nm at a deposition rate of 7.8 Å/s. The sputter target was cleaned for 1 minute before the sputtering process at 150 W.

Membrane electrode assembly.—For the membrane electrode assembly (MEA) fabrication after the Pt deposition, Pt AAO discs were hot pressed onto Nafion membranes (Nafion 212 (50 μm thick) and Nafion XL (25 μm thick) from Fuel Cell Store) at 150°C and 450 N force to form the cathode of the MEA. The cathode was then immersed in 2.0 M NaOH (Sigma Aldrich) to etch the AAO discs, thereby achieving the freestanding Pt nanoelectrode array shown in Figure 1a. Nafion membrane with Pt nanoelectrode array was then protonated by washing the electrode in 0.5 M H_2SO_4 at 80°C for one hour and in DI water at 80°C for one hour as shown in Figure 1b. This step is necessary to ion-exchange Nafion with protons, to remove Na+ ions that exchanged during NaOH etching step. A previous study has shown no enhancement in electrode activity using H_2SO_4 vs. HCl or HNO_3.[2] The cathode MEA with a geometric area of 0.5 cm^2 was built by masking the cathode using a sticky polyimide sheet (Kapton, McMaster Carr) as shown in Figure 1c. The anode was fabricated by painting 40 wt% Pt/C ink with I/C ratio 0.9 on a 5 cm^2 SGL 24BC GDL (Ion Power Inc.). SGL 24 BC was used as the GDL on the cathode side.

Electrochemical MEA testing.—A Scribner fuel cell test station and Biologic VSP potentiostat were used for electrochemical characterization. The cells were conditioned for 8 hours by holding at voltages of 0.7 V, 0.5 V and 0.3 V for 30 s each and repeating over 300 cycles at 60°C and 100% RH in H_2/Air gases. The polarization curves were plotted with current measured by holding each voltage point from 0.8 V to 0.1 V in steps of 0.1 V averaged over 10 minutes.

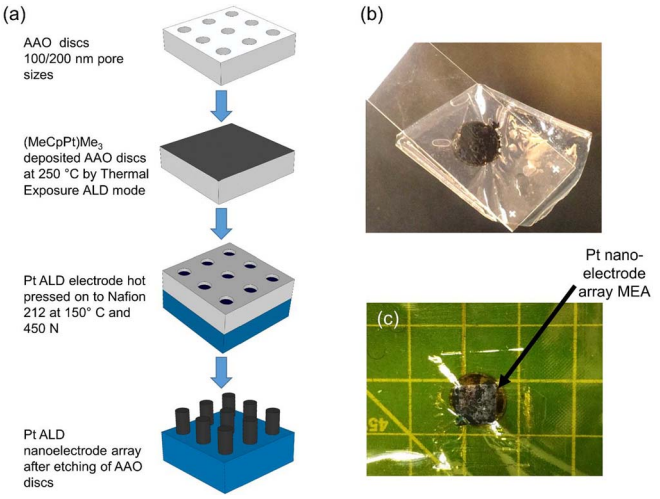

Figure 1. a) ALD process and other post-processing steps in fabricating the nanoelectrode array. b) Pt ALD cathode after protonation, c) cathode side of the electrode after masking with Kapton.

Electrochemical impedance spectroscopy (EIS) was recorded for each voltage step to correct for IR drop, for which resistance was taken at the x-intercept of the Nyquist plot. The frequency range used was 500 kHz to 100 mHz with 6 points per decade spacing and a 5 mV AC perturbation voltage.

ECSA with cycling voltammetry and CO-stripping.—ECSA was calculated from cyclic voltammetry (CV) conducted in a H_2/N_2 environment at different RH at 40°C, with the gas flow-rates of 150 sccm at the anode and 250 sccm at the cathode.

In the MEA configuration 50 cycles of CVs were recorded as "cleaning" CVs, between the range of 0.05 V and 1 V at the sweep rate of 100mV/s. The ECSA was calculated with the charge integrated over the H_{upd}, and divided by the loading L_{Pt} (mg cm^{-2}) and the charge per H_{upd} monolayer:[27,28]

$$ECSA_H = \frac{Q_{H_{upd}}}{210\frac{\mu C}{cm^2} \times L_{Pt}} \quad [1]$$

CO-stripping was conducted by holding a cell voltage of 0.1 V for 30 min. 250 sccm of 2% CO in N_2 mixture was introduced in cathode for 10 min, followed by 300 sccm of N_2 for 20 min. Twenty five voltammograms were recorded at a scan rate of 40 mV/s between 0 V to 1.2 V at a sweep rate of 40 mV/s. In the first anodic scan CO is stripped from the surface by electrooxidation and the charge under the stripping peak is proportional to the CO coverage. The H_{upd} area was calculated after CO-stripping and 25 cleaning cycles. The CO-stripping ECSA was calculated by integrating the charge under the CO-stripping peak, Q_{CO} with respect to the charge for single monolayer[28] and loading L_{Pt} (mg/cm^2):

$$ECSA_{CO} = \frac{Q_{CO,cat}}{420\frac{\mu C}{cm^2} \times L_{Pt}} \quad [2]$$

Here the ECSA calculated with H_{upd} region will be named $ECSA_{CV}$ and with CO-stripping will be named $ECSA_{CO}$.

Results and Discussion

Electrode morphology characterization.—The nanoelectrodes were characterized with Ultra 55 SEM, and the thickness of the electrodes was measured to be 9 μm for 500 cycles of thermal exposure ALD on 200 nm pore AAO discs, as shown in Figure 2a. Figure 2b shows the nanoelectrode array with 500 cycles of thermal exposure ALD on 200 nm pore AAO discs before the etching of the disc, whereas Figure 2c shows a nanoelectrode array in-plane view. The

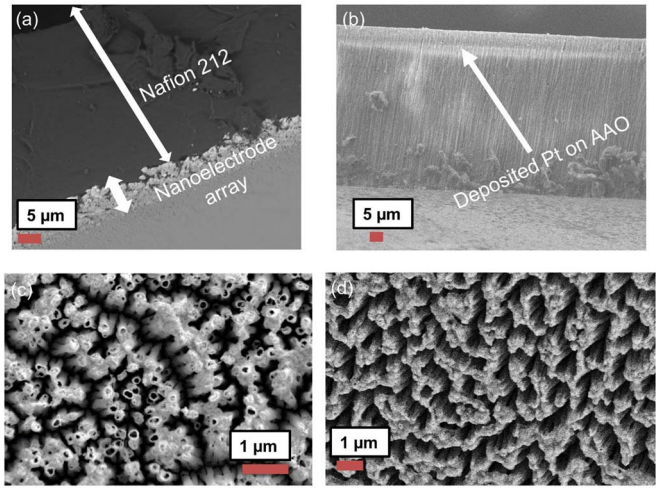

Figure 2. SEM images of the Pt nanoelectrode array: a) after 500 deposition cycles showing a thickness of 9 µm, b) cross sectional side view of Pt deposited onto AAO disk, c) in-plane view of the nanoelectrode array after 300 cycles, d) in-plane view of the nanoelectrode array fabricated using 100 nm pore sized AAO and 200 cycles.

electrode clearly shows Pt hollow tubes that in some locations are bundled together. The deposition was also conducted on 100 nm pore AAO discs and the resulting nanoelectrode arrays are shown in Figure 2d. Bundling of the Pt tubes is undesirable as it inhibits species transport and hence the 200 nm AAO template was adopted for this study. ALD thermal exposure mode with 100 and 200 cycles was also done but the electrodes disintegrated during the etching step. Table I reports the dimensions of the Pt tubes, which are consistent with AAO templates and their areal density of 7 tubes/μm^2, which is lower than 23 tubes/μm^2 calculated for closely packed tubes (see Supplementary Material (SM), Figure S1). The average outer diameter was 218.6 nm for the 200 nm pore sized AAO substrates and 61 nm for the 100 nm pore sized AAO substrates. The Pt thickness for 300 cycles deposition was 28 nm.

Varying precursor exposure time for thickness control.—The diffusion distance of Pt precursor within the pores of the AAO disc varies with exposure time, which for constant diffusion coefficient can be approximated as $L \sim \sqrt{t}$. We performed deposition for exposure times of 2, 5, 7 and 10 seconds. It was difficult to determine the depth of the deposition for the 2 s exposure time from the cross-section SEM image of the AAO disc, as shown by Figure S2a in SM. Higher imaging contrast was achieved after the nanoelectrode array was hot-pressed onto the membrane, where Pt tubular electrode geometry was clearly observed. Thicker depositions were observed with 7 and 10 s exposure times as shown by Figure S2b and c.

From the SEM images of hot-pressed electrode onto the membrane, the electrode thickness was measured, as shown by Figure 3a. The diffusion distance scaling with square root of time is also shown, although this curve can be shifted up or down depending on the multiplication constant. From the plot it is clear that the Pt precursor diffusion distance and electrode thickness does not seem to follow the square-root of exposure time dependency; from these four measurement points the dependency seems to be linear. The deposition process is not just diffusion-controlled but is a coupled diffusion-reaction process. We observe a clear trend in electrode thickness increase with exposure time, where for 2 s exposure the depth of deposition is 4 µm, whereas for 10 s the thickness is 17 µm. Figures 3b and 3c shows sample SEM images used for calculating electrode thicknesses.

Table I. Average Pt parameters calculated from SEM images for 5 s exposure time and 200 nm pore diameters AAO disk.

Parameter	Dimension
Average inner diameter	163.2 ± 6.5 nm
Average outer diameter	218.6 ± 11.9 nm
Average deposition thickness	27.7 ± 9 nm
# of tubes per μm^2 (rounded)	7 ± 1

The performance of the electrode with three deposition exposure times, 2 s, 5 s, and 10 s, was evaluated with polarization curves, and the ECSA was measured with CVs. The discussion of the optimization of the PEFC operating conditions is discussed in the SM. Figure 4 compares polarization behavior of the three electrodes without ionomer and one that contains 0.1wt% Nafion (5s exposure time). The cell with 2 s exposure time showed 0.9 V OCV but dramatically low current densities. The cells with nanoelectrode array deposited with 5 and 10 s exposure times showed similar behavior in the low current density region (< 50 mA cm^{-2}) but the second cell achieved almost twice amount of current density (400 mA cm^{-2}) at 0.1 V compared to the first one. Lastly, the PEFC with 0.1wt% of Nafion had the highest current densities in all potential regions, reaching a maximum value of 500 mA cm^{-2} at 0.1 V. The only difference between this electrode and the one with 5 s exposure time is the presence of ionomer. A 2.5 factor of improved current densities at low potential is most likely due to proton transport effects. Similar trends are observed for iR- corrected data, as shown by Figure 4b.

The $ECSA_{CV}$ values were the highest at 10 and 11 $m^2\ g_{Pt}{}^{-1}$ for electrodes prepared with 5 s ALD exposure time with and without ionomer, respectively. These two values confirm that Pt is accessible in the H_{upd} region with or without ionomer. Previous studies have shown H_{ad} surface diffusion and proton migration as possible mechanisms for protons to access Pt, which is not directly in contact with ionomer.[15,19,20,22,23] It is already known that Pt accessibility in H_{upd} region does not necessarily translate into Pt accessibility at current densities in ORR region.[21] Under high current densities proton-transport limitations can become significant in ionomer-free electrodes.

Electrodes fabricated with 2 s and 10 s ALD exposure times showed lower $ECSA_{CV}$ values of 2 and 3 $m^2 g_{Pt}{}^{-1}$, respectively. The electrode with 2 s exposure time showed both low $ECSA_{CV}$ and low current densities indicating that 2 s exposure time of Pt precursor is not sufficient to produce stable and functioning electrodes. The electrode with 10 s exposure time has higher loading (0.625 mg cm^{-2}) than that at 5 s (0.52 mg cm^{-2}) but loading only does not explain the low $ECSA_{CV}$ value. The electrode thickness of 17 µm is large, and without ionomer $ECSA_{CV}$ accessibility can be impaired as protons are reactants in H_{upd} reaction, as discussed later in the manuscript.[15,24,29] When current is normalized per loading of Pt, the 5 s exposure time electrodes showed the highest performance, as shown by Figure 4d.

Ionomer-free Pt ALD nanoelectrode RH dependency.—Figure 5a shows polarization curves for the Nafion-free nanoelectrode array with 5 s exposure time deposition at various RHs. A clear trend is observed, where dramatic decrease in current density occurs with decrease in RH for the full potential range. As shown by the Figure 5b inset, the open circuit potential (OCV) is also quite sensitive to the change in the RH, where the highest value is reached at a fully humidified condition. This might be due to the reduced hydrogen crossover at high RH conditions as the solubility of H_2 gas decreases with increase in wetting of the membrane and hence permeability of gas is reduced.[30–32]

Figure 5b shows high frequency resistance (HFR) at three applied potentials for a range of RH values. As potential decreases, all the HFRs also decrease. The HFR increases with decrease in RH, which is due to membrane and ionomer ionic conductivity dependence on RH. Steinbach et al.[33] developed a theory to explain both ionomer-free and ionomer-containing electrodes' performance dependency on RH. The underlying hypothesis is that the decrease in current density with RH is due to reduction in the utilized active area of the MEA. The increase in HFR is due to decrease in membrane conductive area, a decrease of ionically conductive pathways between membrane and electrode. For ionomer-free electrodes at low RH, it is not clear what the mechanisms

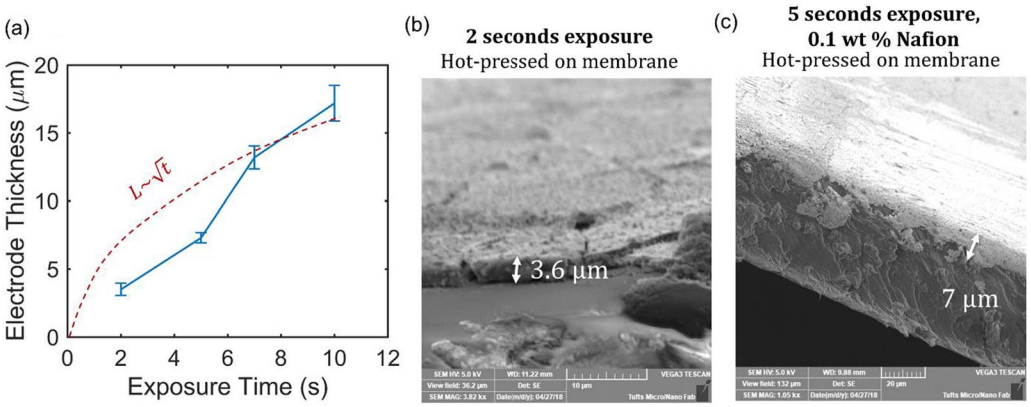

Figure 3. a) Plot of electrode thickness vs exposure time b) through plane view of sample with 2s exposure time after 500 cycles c) through plane view of sample with 5s exposure time after 500 cycles coated with 0.1wt.% Nafion and hot-pressed onto membrane.

of proton transport through these electrodes are. Here, we hypothesize that adsorbed water films at higher RH and lower applied potentials enhance proton conductivity of these electrodes, enabling higher Pt utilization.[12]

Figure 6a shows polarization curves for the nanoelectrode array with 10 s precursor exposure time deposition and at four RH conditions. From 50 to 100% RH similar behavior was observed as was shown before for electrodes with 5 s exposure time: increase in current density with increase in RH. Once overhumidified gas at 120% RH was supplied to the cell, significant performance increase was observed. At 0.2 V current density doubled compared to 100% RH (from 400 mA cm^{-2} to 800 mA cm^{-2}). This performance enhancement is observed for a full range of potentials, not just at high current density. From HFR data (Figure 6b) the HF impedance is similar for 100% and 120%, at around 0.2 Ohm cm^2. From cyclic voltammetry plots, at 100% and 120% RH the $ECSA_{CV}$ values are equivalent and calculated to be 3 m^2 $g_{Pt}{}^{-1}$. From HF resistance and $ECSA_{CV}$ values one cannot determine the reason for doubling of current density at 120% RH compared to 100% RH. For lower RH both HFR is higher and also $ECSA_{CV}$ values are about half of those at fully humidified condition.

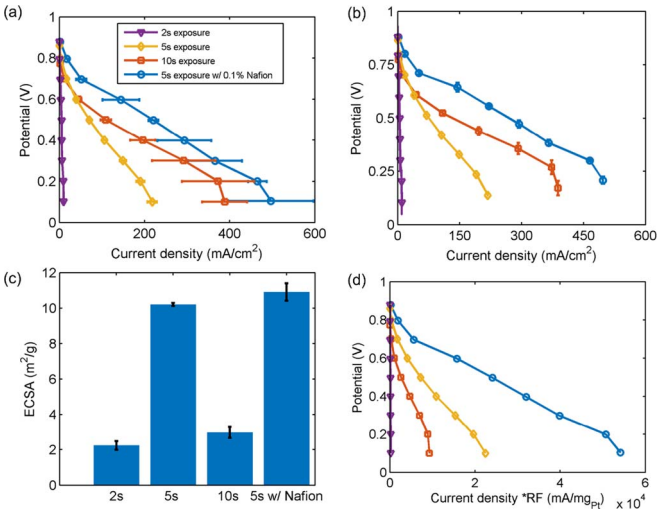

Figure 4. a) Polarization curve and b) ir-free polarization curve for ALD electrodes with varied precursor exposure time during deposition, c) $ECSA_{CV}$ vs exposure time for the four electrodes (three ionomer-free and one with ionomer), d) potential vs. specific current density for nanoelectrodes with 2s, 5s and 10s exposure time, and nanoelectrode w/ Nafion. The testing conditions were 80°C, 100% RH and 100kPa backpressure, 0.2 slpm H_2 at anode and 0.4 slpm air at cathode.

For all four RHs the oxide region in the CV is not well-pronounced up to 1 V. $ECSA_{CO}$ is also calculated from the CO-stripping experiment (Figure 6d), after CO adsorption at potential hold at 0.1 V. The $ECSA_{CO}$ for 100% RH was found to be 4 m^2 $g_{Pt}{}^{-1}$. Higher values of $ECSA_{CO}$ compared to $ECSA_{CV}$ have been reported in literature before; the origin of the difference is currently not well understood.[34] In the CO-stripping experiment protons are reaction products and numerous studies have shown that CO oxidation on noble metals follows the Langmuir-Hinshelwood mechanism.[35] The following equations describe the electrochemical CO oxidation:

$$H_2O + * \leftrightarrow OH_{ad} + H^+ + e^- \quad [3]$$

$$OH_{ad} + CO_{ad} \rightarrow COOH_{ad} \quad [4]$$

$$COOH_{ad} \rightarrow CO_2 + H^+ + e^- + * \quad [5]$$

In Eq. 3 formation of OH_{ad} consists of adsorption of water onto a free site, "*". In the second step CO_{ad} and OH_{ad} both need to be present on the surface for the reaction to proceed. Various models exist to explain kinetics of the reaction, taking into account mobility of one or both of the adsorbates. The rate-determining step is Eq. 4, which depends on the availability of the OH_{ad}, indicating that it is also an RH-dependent step.

For the H_{upd} on Pt surface, the surface reaction depends on protons:

$$Pt + H_3O^+ + e^- \leftrightarrow Pt - H_{upd} + H_2O \quad [6]$$

The reaction dependency on proton availability perhaps differentiates the ECSA values measured with CV and CO-stripping. Similar to CV the ORR depends on proton availability and hence $ECSA_{CV}$ can be a more realistic metric of Pt active area accessible to protons, whereas $ECSA_{CO}$ can be more of an ideal value, that might not be accessible

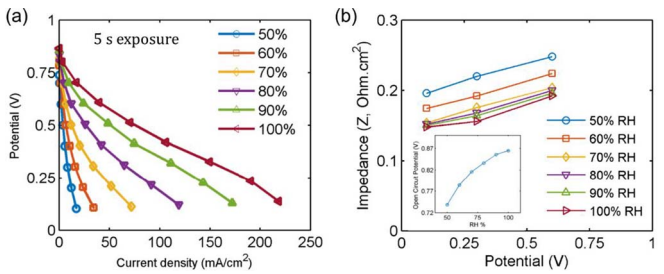

Figure 5. a) Polarization curve of a Pt ALD electrode as a function of RH at 80°C with 100 kPa backpressure. The results are IR-corrected. B) Impedance plot for a range of potentials and RHs, the inset shows the variation of OCV with RH.

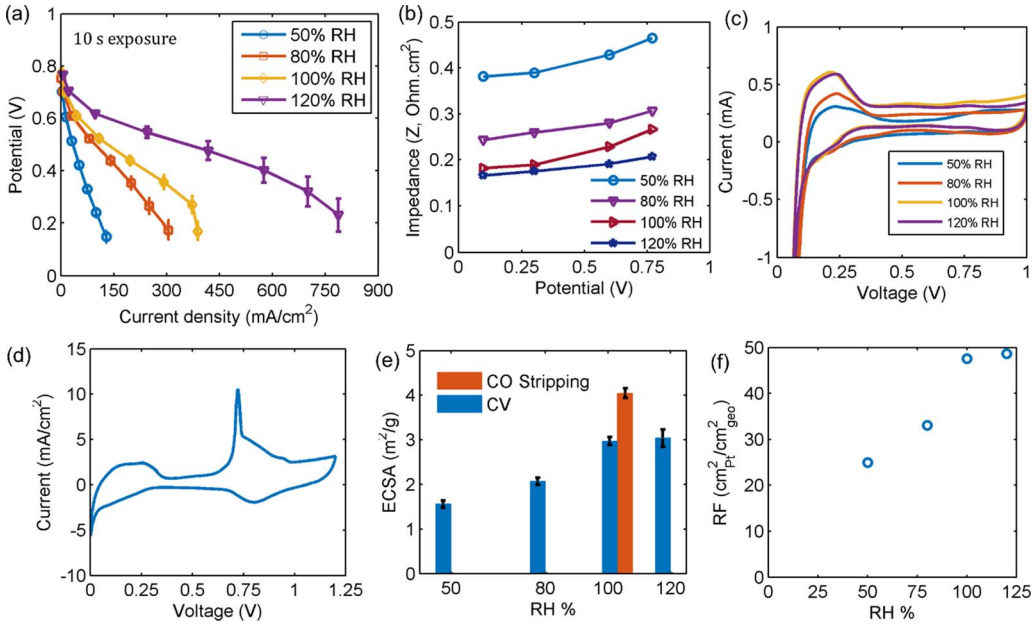

Figure 6. For ALD sample with 10s exposure time and 500 cycles a) polarization curves at 80°C, hydrogen gas at anode and air at cathode, 100 kPa backpressure at various RH b) HFR resistance vs potential at various RH, c) CV at four RH conditions at 40°C d) CO-stripping curve measured at 40°C, 100% RH e) ECSA measured from CV techniques vs RH%, f) Roughness factor vs RH. Electrode active area is 0.25 cm^2.

during ORR due to lack of protons. The roughness factor plot is shown by Figure 6f, where roughness factor is proportional to ECSA because geometric area of the cell remains the same.

Ionomer containing Pt ALD nanoelectrode RH dependency.— Figure 7a shows polarization curves for the ionomer-containing nanoelectrode array at three RHs: 50, 100 and 120%. Similarly to the ionomer-free electrode the RH dependence is significant from 50 to 100% RH. Different behavior is observed for 120% RH compared to the behavior at 120% RH for the ionomer-free electrode. Here, the current densities for 100 and 120% RH from OCV to 0.5 V are identical, indicating that overhumidification does not increase performance in this low current density range. After 0.5 V the current density takes off for 120% RH and is close to 750 mA cm^{-2} at 0.2 V compared to 500 mA cm^{-2} at 100% RH. This current "ignition" was previously observed by Gasda et al.[36] and also Babu et al.[37] for ionomer-free electrodes, attributed to water wetting the ionomer-free regions increasing current density, which produces more water and increases proton conductivity. Here, it is not clear whether ionomer penetrates the nanoelectrode array completely or partially. Ionomer can also improve interface between nanoelectrode array and membrane. The HFR for this ionomer-containing

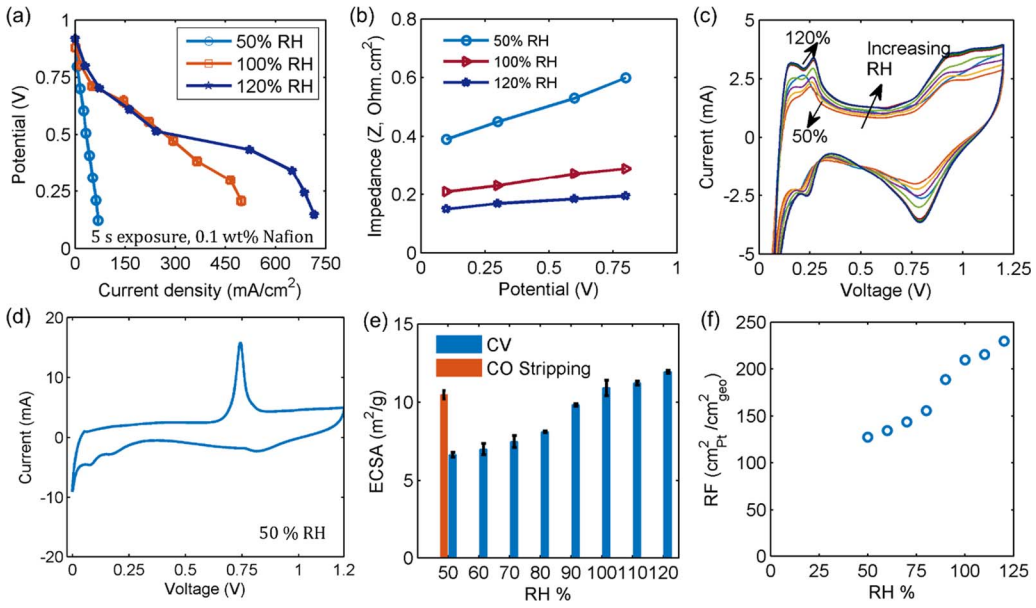

Figure 7. ALD nanoelectrode array fabricated with 5s exposure time and 500 cycles, 0.1wt% Nafion was used during electrode fabrication. a) Polarization curves at 80°C, hydrogen gas at anode and air at cathode, 100 kPa backpressure at various RH, b) HFR for four applied potentials and three RHs, c) CV at various RH conditions and d) CO stripping at 50% RH, 40°C and no backpressure e) ECSA measured from CO-stripping and CV techniques vs RH, e) Roughness factor vs RH. The electrode active area is 0.5 cm^2.

Table II. Comparison of experimental and theoretical parameters for ALD nanoelectrode fabricated with 5 s precursor exposure time.

Parameter	Measured experimentally (5 s exposure, 0.1 wt% Nafion, 100% RH)	Calculated (Hollow tubes)	Calculated (Non hollow tubes)
Loading (mg cm^{-2})	0.52	0.91	2.06
$ECSA_{CV}$ (m^2 g^{-1})	10.9	12.1	7.45
Roughness Factor (cm^2 $_{Pt}$ cm^{-2} $_{geo}$)	209.7	242.0	149.1

electrode is shown by Figure 7b and is very similar to that of an ionomer-free electrode. The cyclic voltammetry curves are very different in shape compared to the ionomer-free electrode. Two peaks in H_{upd} region are clearly observed, whereas for ionomer-free electrode these peaks were only observed in the reverse scan of the CV. Moreover, the onset for oxide growth is ~0.8 V, with surface oxides reduction peak at around 0.78 V for all RHs. The 100 and 120% RH show identical CVs and almost the same $ECSA_{CV}$ as shown from Figures 7c and 7e. The CO-stripping was performed only at 50% RH and a clear peak is observed at 0.8 V. The $ECSA_{CO}$ was 1.4 times higher than that from CV. We will explore the ECSA ratios from CO-stripping and CV in the next section. High roughness factors were observed reaching 230 cm^2_{Pt} cm^{-2}_{geo} at 120% RH.

Pt utilization within ALD nanoelectrode array.—To approximate Pt utilization in these electrodes we performed back-of-the-envelope calculations using SEM images for nano-tubes density of 7 tubes μm^{-2} and electrode thickness 7.3 μm with active area of 0.5 cm^2. These conditions were for the ALD nanoelectrode array with 5 s precursor exposure time. The calculations were performed by assuming either hollow or filled Pt tubes. The hollow tube parameters are reported in Table I. For the filled Pt tubes only external surface area was counted toward the ECSA. Table II compares the experimental measurements for 100% RH (as reported by Figure 4) and theoretical calculations. Theoretical calculations of the ECSA if all Pt within hollow nanoelectrode array was accessible is 12.1 m^2 g^{-1}, whereas if Pt array was not hollow it would be 7.45 m^2 g^{-1}. The experimental data for ionomer-containing electrode has ECSA value of 10.9 m^2 g^{-1}, whereas for ionomer-free electrode it is 10 m^2 g^{-1} (Figure 4c). By dividing actual ECSA by the theoretical, Pt utilization can be calculated to be 90% for ionomer-containing electrode and 77% for ionomer-free at 100% RH condition. This is indicative that almost full length of the electrode is accessed during the ECSA measurement.

The success rate of fabricating the electrodes and having them electrochemically active within the PEFC hardware was around 1 in 3. The post-mortem SEM analysis of well-performing vs. poor-performing electrodes showed a similar trend. Figure 8 shows SEM images of a well-performing electrode and a poor-performing electrode. Clustering of whiskers was observed for the electrode that produced < 50 mA cm^{-2}, whereas well-performing electrodes showed well-dispersed hollow Pt tubes.

Model electrodes as a platform to study transport-dependent ECSA accessibility.—For this study several electrode configurations were fabricated with or without Au interlayer to probe ECSA detectability with two methods for a RH-range, as was earlier done by McBreen[18] for 100% RH and CV only. The ionomer-free Pt ALD electrode fabricated with 5 s exposure time and 300 cycles was sandwiched between the membrane and the gas diffusion electrode (GDE). As shown by Table III the loading of the GDE was 0.21 mg cm^{-2} and the loading of the Pt ALD was 0.29 mg cm^{-2}. The combined electrode loading was taken to be the sum of both. McBreen has previously shown that when combining two Pt ionomer-free screens the charge from H_{upd} region doubled, however they have not translated the values into the ECSA. If the loading of the screens is the same, doubling the charge, Q, and doubling the loading, L_{Pt}, results in unchanged ECSA. Here, the CV plots for combined electrodes at 100% RH and 40°C are shown in SM, Figure S5. For all three cases, strongly and weakly adsorbed H_{upd} peaks are observed. The calculated ECSA values for 100% RH are 5.9, 9.52 and 6.41 m^2 g^{-1}_{Pt} for Pt ALD, Pt/C GDE, and a combination of both, respectively (Table III). Table III shows the GDE, Pt ALD and combined electrodes' charges from H_{upd} region, which were 4.2, 3.6 and 6.73 mC cm^{-2}, respectively. If the combined electrode was fully utilized then the charge from H_{upd} region should be a sum of charges from GDE and Pt ALD, which is 7.8 mC cm^{-2}. The measured charge of 6.73 mC cm^{-2} indicates that not all Pt in the combined electrode is utilized, and by dividing this by the calculated number, the utilization is 86.2%. Similarly, for full utilization the combined electrode's $ECSA_{CV}$ should be 7.4 m^2_{Pt} g^{-1}, which is higher than the measured $ECSA_{CV}$.

Table III. Representative loading, H_{upd} charge and ECSA for GDE, Pt ALD and combined at 100% RH.

	Loading [mg_{Pt} cm^{-2}]	Q [mC cm^{-2}]	ECSA [m^2 g^{-1}]
GDE	0.21	4.2	9.52
Pt ALD	0.29	3.6	5.9
Combined	0.50	6.73	6.41

ECSA as a function of RH for three types of electrodes is plotted in Figure 9 over the range of 50%–100% RH. Figure 9a plots $ECSA_{CV}$, whereas Figure 9b plots $ECSA_{CO}$. The tabulated values for the ECSA are shown in SM Tables S3 and S4. The corresponding values for the integrated charge from the H_{upd} region in CV and CO-stripping are shown by Figures 9c and 9d, respectively. For all three composite electrodes severe RH dependency was observed with both CV and CO-stripping methods. The ECSA values for Pt ALD on Pt/C electrode had similar values with both CV and CO-stripping methods for the

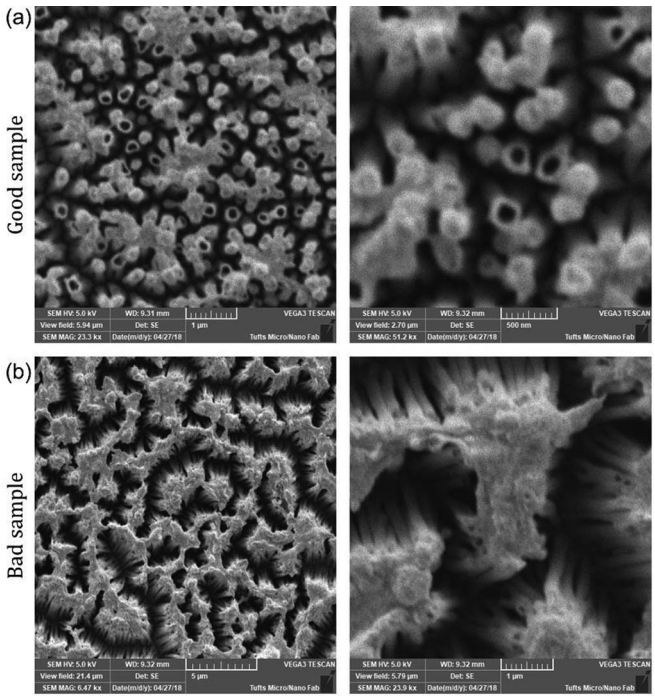

Figure 8. A post-mortem SEM image of a) well-performing electrode and b) electrode that produced current density of < 50 mA cm^{-2} for a full potential range.

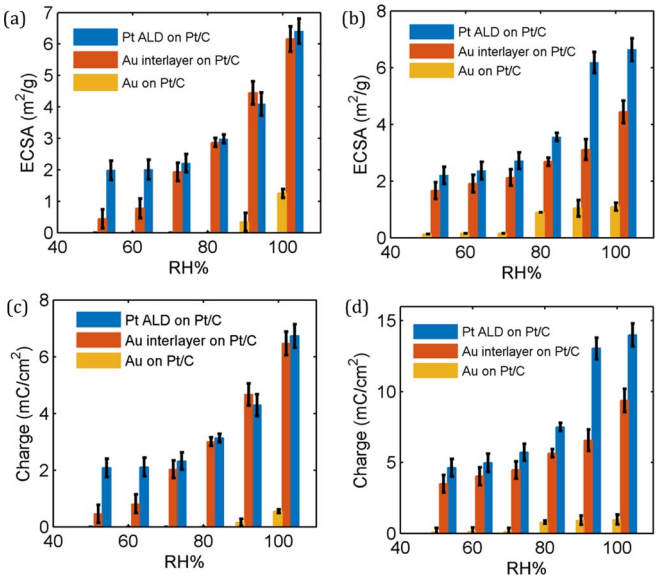

Figure 9. Plot of the ECSA dependence on the RH for three electrodes calculated with a) CV and b) CO-stripping. The charge calculated from the c) H_{upd} and d) CO-stripping.

RH range. Figure 9 shows that for Au interlayer between membrane and Pt/C the ECSA values with both techniques is negligibly low, indicating that Pt in direct contact with membrane is needed to initiate the reaction. Low values of current density with Au interlayer were observed by Hu et al. with a similar trend in $ECSA_{CV}$ dependency with RH.[16]

The presence of the Au interlayer between Pt ALD and Pt/C GDE does not alter $ECSA_{CV}$ at high RHs (70% and above) as seen from Figure 9a. From the raw CV data, it is apparent that Au distorts the CV and introduces transport limitations (observed in the H_{upd} peak shifts), as shown in SM Figure S5 and as also shown previously by McBreen.[18] Proton migration could be the possible transport mechanism in $ECSA_{CV}$ detection, as partial ECSA of the GDE could be detected through the proton migration across the Au interlayer. In this low potential region Pt is charged negatively or close to neutral, as the pzc of Pt is 0.23 V[38] and proton migration in the electric double layers (EDLs) is a feasible mechanism.[15,23] Water is required for proton migration and hence decrease in the $ECSA_{CV}$ with Au interlayer is more pronounced at low RH. This decrease is not as pronounced for Pt ALD on the Pt/C because Pt/C portion of the electrode contains ionomer and its access is not inhibited by Au interlayer.

When including Au interlayers, the $ECSA_{CO}$ of the electrode with Au interlayer decreases at 90 and 100% RH compared to Pt ALD on Pt/C without Au interlayer. There are two factors contributing to the $ECSA_{CO}$ decrease: 1) on the Au surface, the electrosorption of CO is relatively weak[39,40] and 2) the onset of OH formation on the Au surface occurs at much higher potentials. Here the potential sweep was conducted only up to 1 V and the CO oxidation at higher potentials was not captured. Previous studies have shown that in the presence of Au nano-particles the CO electrooxidation peak shifts to higher potentials (even higher than 1 V),[41,42] which is most likely due to OH binding occurring at higher potentials. From Eq. 4 both CO and OH are needed to complete CO-oxidation reaction. However, the drop-off of the $ECSA_{CO}$ for the electrode with Au-interlayer at lower RH ($< 90\%$) was not as large compared to the $ECSA_{CV}$ drop-off. Protons are not reactants in the $ECSA_{CO}$ and this might be the reason for higher $ECSA_{CO}$ than $ECSA_{CV}$ at low RH.

Conclusions

This paper presents a method for controlled and uniform deposition of Pt onto high aspect-ratio substrates using atomic layer deposition (ALD) with thermal exposure mode. Due to controlled geometry these ionomer-free electrodes serve as model systems for studying ion transport mechanisms. By varying precursor exposure time during ALD process electrode thickness was controlled. The maximum depth of deposition was 17 μm, and these electrodes showed comparably high ECSA and similar current densities in comparison to previous findings.[2,43] Due to a lack of ionomer phase, these electrodes showed significant dependence on the relative humidity (RH). The maximum performance was achieved at overhumidified condition with 120% RH and at low potentials. A current density jump was observed at 120% RH relative to 100% RH for both ionomer-containing and ionomer-free electrodes at low applied potentials. This can be attributed to ignition currents due to higher generated amounts of water and improved ionic conduction. Pt utilization in these electrodes was approximated by comparing measured ECSA values from those calculated from geometric area. Pt utilization was shown to be 90% for ionomer-containing electrodes and 77% for ionomer-free electrodes at 100% RH condition.

Pt ALD electrodes were used as model systems to study species transport during ECSA determination with both cyclic voltammetry (CV) and CO-stripping. Stacking Pt ALD and Pt/C GDE showed that Pt accessibility is about 86%. Using Au interlayer between Pt ALD and Pt/C conventional GDEs, we were able to delineate transport mechanisms by studying ECSA dependency on RH with CV and CO-stripping techniques. Both methods showed dependency of the ECSA on the RH. Hydrogen surface diffusion showed not to be the dominant transport mechanism in CV detection due to several reasons: 1) strong RH-dependency, and 2) the Au interlayer not acting as a blocking surface in the CV experiment. The study indicates that surface migration is the likely mechanism for proton transport in ionomer-free electrodes.

Acknowledgments

This material is based upon work supported by the National Science Foundation under grant No. 1652445. We thank Sean Chapman and Jake Berliner for helping with ALD electrode characterization and Berney Peng for SEM sample preparation. Fabrication of the structures was carried out in part at the Tufts Micro and Nano Fabrication Facility. This work was performed in part at the Center for Nanoscale Systems (CNS), a member of the National Nanotechnology Coordinated Infrastructure Network (NNCI), which is supported by the National Science Foundation under NSF award no. 1541959. CNS is part of Harvard University.

ORCID

Iryna V. Zenyuk https://orcid.org/0000-0002-1612-0475

References

1. S. Shukla, K. Domican, K. Karan, S. Bhattacharjee, and M. Secanell, *Electrochim Acta*, **156**, 289 (2015).
2. S. Galbiati, A. Morin, and N. Pauc, *Electrochim Acta*, **125**, 107 (2014).
3. M. Inaba, T. Suzuki, T. Hatanaka, and Y. Morimoto, *Journal of The Electrochemical Society*, **162**, F634 (2015).
4. Z. Q. Tian, S. H. Lim, C. K. Poh, Z. Tang, Z. Xia, Z. Luo, P. K. Shen, D. Chua, Y. P. Feng, Z. Shen, and J. Lin, *Advanced Energy Materials*, **1**, 1205 (2011).
5. W. Zhang, A. I. Minett, M. Gao, J. Zhao, J. M. Razal, G. G. Wallace, T. Romeo, and J. Chen, *Advanced Energy Materials*, **1**, 671 (2011).
6. T. Fujigaya and N. Nakashima, *Advanced Materials*, **25**, 1666 (2013).
7. M. K. Debe, A. K. Schmoeckel, G. D. Vernstrom, and R. Atanasoski, *Journal of Power Sources*, **161**, 1002 (2006).
8. M. K. Debe, *Nature*, **486**, 43 (2012).
9. M. K. Debe, *Journal of Electrochemical Society*, **159**, B53 (2012).
10. M. K. Debe, *Journal of Electrochemical Society*, **160**, F522 (2013).
11. A. Kongkanand and P. K. Sinha, *Journal of Electrochemical Society*, **158**, B703 (2011).
12. P. K. Sinha, W. Gu, A. Kongkanand, and E. Thompson, *Journal of Electrochemical Society*, **158**, B831 (2011).
13. E. F. Medici, I. V. Zenyuk, D. Y. Parkinson, A. Z. Weber, and J. S. Allen, *Fuel Cells*, **16**, 725 (2016).

14. I. V. Zenyuk, P. K. Das, and A. Z. Weber, *Journal of Electrochemical Society*, **163**, F691 (2016).
15. I. V. Zenyuk and S. Litster, *Electrochim Acta*, **146**, 194 (2014).
16. L. Hu, M. Zhang, S. Komini Babu, and S. Litster, *Ecs Transactions*, **75**, 339 (2016).
17. K. C. Hess, W. K. Epting, and S. Litster, *Analytical Chemistry*, **83**, 9492 (2011).
18. J. McBreen, *Journal of Electrochemical Society*, **132**, 1112 (1985).
19. W.-Y. Tu, W.-J. Liu, C.-S. Cha, and B.-L. Wu, *Electrochim Acta*, **43**, 3731 (1998).
20. W.-J. Liu, B.-L. Wu, and C.-S. Cha, *Journal of Electroanalytical Chemistry*, **476**, 101 (1999).
21. S. Tominaka, C.-W. Wu, K. Kuroda, and T. Osaka, *Journal of Power Sources*, **195**, 2236 (2010).
22. U. A. Paulus, Z. Veziridis, B. Schnyder, M. Kuhnke, G. G. Scherer, and A. Wokaun, *Journal of Electroanalytical Chemistry*, **541**, 77 (2003).
23. K. Chana and M. Eikerling, *Journal of Electrochemical Society*, **158**, B18 (2011).
24. I. V. Zenyuk and S. Litster, *The Journal of Physical Chemistry C*, **116**, 9862 (2012).
25. M. Steinhart, R. B. Wehrspohn, U. Gösele, and J. H. Wendorff, *Angewandte Chemie International Edition*, **43**, 1334 (2004).
26. W. Lee, R. Scholz, K. Nielsch, and U. Gösele, *Angewandte Chemie International Edition*, **44**, 6050 (2005).
27. S. Trasatti and O. A. Petrii, Real surface area measurements in electrochemistry, in *Pure and Applied Chemistry*, p. 711 (1991).
28. T. Binninger, E. Fabbri, R. Kötz, and T. J. Schmidt, *Journal of Electrochemical Society*, **161**, H121 (2014).
29. I. V. Zenyuk, J. Lee, and S. Litster, *Ecs Transactions*, **41**, 179 (2011).
30. S. S. Kocha, J. Deliang Yang, and J. S. Yi, *AIChE Journal*, **52**, 1916 (2006).
31. X. Cheng, J. Zhang, Y. Tang, C. Song, J. Shen, D. Song, and J. Zhang, *Journal of Power Sources*, **167**, 25 (2007).
32. A. Z. Weber and J. Newman, *Journal of Electrochemical Society*, **151**, A326 (2004).
33. A. J. Steinbach and D. M. Peppin, *ECS Transactions*, **58**, 1589 (2013).
34. S. Taylor, E. Fabbri, P. Levecque, T. J. Schmidt, and O. Conrad, *Electrocatalysis*, **7**, 287 (2016).
35. F. Maillard, M. Eikerling, O. Cherstiouk, S. Schreier, E. Savinova, and U. Stimming, *Faraday discussions*, **125**, 357 (2004).
36. M. Gasda, G. Eisman, and D. Gall, *Journal of the Electrochemical Society*, **157**, B437 (2010).
37. S. K. Babu, R. W. Atkinson III, A. B. Papandrew, and S. Litster, *chemelectrochem*, **2**, 1752 (2015).
38. A. Ganassin, P. Sebastián, V. Climent, W. Schuhmann, A. S. Bandarenka, and J. Feliu, *Scientific Reports*, **7**, 1246 (2017).
39. S. C. Chang, A. Hamelin, and M. J. Weaver, *The Journal of Physical Chemistry*, **95**, 5560 (1991).
40. G. J. Edens, A. Hamelin, and M. J. Weaver, *The Journal of Physical Chemistry*, **100**, 2322 (1996).
41. G.-R. Zhang, D. Zhao, Y.-Y. Feng, B. Zhang, D. S. Su, G. Liu, and B.-Q. Xu, *ACS Nano*, **6**, 2226 (2012).
42. Q. Zhang, R. Yue, F. Jiang, H. Wang, C. Zhai, P. Yang, and Y. Du, *Gold Bulletin*, **46**, 175 (2013).
43. S. Galbiati, A. Morin, and N. Pauc, *Applied Catalysis B: Environmental*, **165**, 149 (2015).